Journal of Environmental Chemical Engineering 11 (2023) 110018

Contents lists available at ScienceDirect

Journal of Environmental Chemical Engineering

journal homepage: www.elsevier.com/locate/jece

On the role of the nature and density of acid sites on mesostructured aluminosilicates dehydration catalysts for dimethyl ether production from CO_2

Fausto Secci [a], Valentina Mameli [a,b], Elisabetta Rombi [a,b], Sarah Lai [c], Marco Sanna Angotzi [a,b], Patrícia A. Russo [d], Nicola Pinna [d], Mauro Mureddu [c], Carla Cannas [a,b,*]

[a] Department of Chemical and Geological Sciences, University of Cagliari, S.S. 554 bivio per Sestu, 09042 Monserrato, CA, Italy
[b] Consorzio Interuniversitario Nazionale per la Scienza e Tecnologia dei Materiali (INSTM), Via Giuseppe Giusti 9, 50121 Firenze, FI, Italy
[c] Sotacarbo S.p.A., Grande Miniera di Serbariu, 09013 Carbonia, SU, Italy
[d] Institut für Chemie and IRIS Adlershof, Humboldt-Universität zu Berlin, 12489 Berlin, Germany

ARTICLE INFO

Editor: Dr. G. Palmisano

Keywords:
Mesostructured catalysts
Brønsted sites
Lewis sites
Site density
NH_3 microcalorimetry
Pyridine-FTIR

ABSTRACT

In this work, we designed four different mesostructured acidic materials to be used as methanol dehydration catalysts for the one-pot CO_2-to-DME process, in the form of physical mixtures with a Cu/ZnO/Al_2O_3-based commercial redox catalyst (CZA). The studied systems consist in a mesostructured γ-Al_2O_3 and three mesostructured aluminosilicates (namely Al-MCM-41, Al-SBA-15, and Al-SBA-16) with the same Si/Al ratio (= 15) but significantly different textural properties. The main goal of this work is to understand how the textural features can influence the acidic properties (typology, amount, strength, surface density) and, consequently, how catalytic performances can be correlated with acidic features. On this note, we found that the systems presenting both Brønsted and Lewis sites (namely the three aluminosilicates) show much better catalytic performances than γ-Al_2O_3, that only features Lewis sites, thus implying that Brønsted sites are more active towards methanol dehydration than Lewis sites. The three aluminosilicates, despite presenting comparable amounts of Brønsted sites, show significantly different performances in terms of selectivity to DME; particularly, Al-SBA-16, the system with the lowest surface area, proved to be the most efficient catalyst. This finding led us to infer that, besides Brønsted acidity, a high surface density of acid sites is a key factor to obtain a high dehydration activity; being methanol dehydration a bi-molecular reaction, the close proximity of two acid sites would indeed favor the kinetics of the process.

1. Introduction

During the latest decades, the consequences brought by the rapid increase of global CO_2 emission have been a very hot topic in the whole scientific community. CO_2 is indeed widely acknowledged as the main responsible for global warming, due to its greenhouse effect. Therefore, the attention of the scientists has been focused on the research of new green fuels. Among them, dimethyl ether (DME), due to its peculiar features, has gathered an increasing attention. DME, indeed, can be stored and transported using the same technologies used nowadays for LPG (liquefied petroleum gas). Furthermore, it can be used as an additive to diesel fuel, improving the performances of the engines due to its high cetane number and, after proper modifications to engines, it can completely replace diesel fuel, producing less emissions of particulate, aromatic compounds, NO_x, and SO_x [1–10]. The industrial production of DME is usually performed from syngas; however, the research has recently devoted efforts to the CO_2-to-DME process, which allows to obtain DME re-evaluating CO_2 as a reagent rather than as a waste [1,4,7,11]. This process can thus be considered as a part of the Carbon Capture and Utilization (CCU) framework. CO_2 transformation into DME consists in two subsequent reactions [1,6,12]. The first one is the reduction of CO_2 to methanol in the presence of hydrogen:

$$CO_2 + 3H_2 \rightleftarrows CH_3OH + H_2O$$

The second one consists in the dehydration of methanol to DME:

* Corresponding author at: Department of Chemical and Geological Sciences, University of Cagliari, S.S. 554 bivio per Sestu, 09042 Monserrato, CA, Italy.
E-mail address: ccannas@unica.it (C. Cannas).

https://doi.org/10.1016/j.jece.2023.110018
Received 28 January 2023; Received in revised form 24 April 2023; Accepted 26 April 2023
Available online 27 April 2023
2213-3437/© 2023 The Authors. Published by Elsevier Ltd. This is an open access article under the CC BY license (http://creativecommons.org/licenses/by/4.0/).

$$2CH_3OH \rightleftarrows CH_3OCH_3 + H_2O$$

The global reaction, thus, results to be:

$$2CO_2 + 6H_2 \rightleftarrows CH_3OCH_3 + 3H_2O$$

In this process, CO_2 reduction to methanol competes with the Reverse Water-Gas Shift (RWGS) reaction, that gives rise to the formation of CO:

$$CO_2 + H_2 \rightleftarrows CO + H_2O$$

The catalytic systems used for the CO_2-to-DME process are similar to those used for the DME production from syngas. Cu-based catalysts are, by far, the most widely reported systems for the promotion of the CO_2 reduction to methanol. In these catalysts, Cu is often paired with one or more promoters, among which ZnO is one of the most widely used; its role consists in increasing the dispersion of the active phase, acting as a spacer between the copper particles. Cu/ZnO catalysts often feature the presence of a third phase, usually Al_2O_3 or ZrO_2, which increases the thermal and chemical stability of the catalyst, granting more stable performances [1,6,9,12,13]. Regarding methanol dehydration to DME, a wide range of solid acidic catalysts have been reported in the literature. One of the most used is γ-Al_2O_3, mainly due to its low cost compared to other more active dehydration catalysts, like zeolites. However, γ-Al_2O_3 tends to lose performances over time, due to deactivation of its Lewis acid sites (the only type of acid sites present on this catalyst) caused by the adsorption of water molecules produced during the reaction, forming a Lewis acid-base adduct [13,14]. This downside of γ-Al_2O_3 is particularly problematic for the CO_2-to-DME process – which is the focus of this work– due to the formation, for each DME molecule, of three water molecules that can adsorb on the Lewis acid sites of γ-Al_2O_3, competing with methanol and deactivating the sites. In a previous study [15], also supported by literature results from other authors [16,17], we observed how Brønsted sites, compared to Lewis sites, showed much higher water resistance and, consequently, better performances for methanol dehydration. In this context, zeolites, bearing Brønsted acid sites, have proven to be better catalysts for methanol dehydration, also due to the lower hydrophilicity of their surface [16,17]. Ideal Brønsted acid sites, however, need to show a moderate or weak strength, since the presence of strong sites could lead to the formation of olefins through the MTO (methanol-to-olefins) process [17]. So far, in addition to zeolites and γ-Al_2O_3, few cases of mesoporous and mesostructured acid catalysts have been reported in the literature for the synthesis of DME, despite their potential for the development of bifunctional nanocomposite catalysts [15].

Like in the case of the syngas-to-DME process, the CO_2-to-DME process is often performed through a one-step route by the use of two-function catalytic systems, containing both the redox and the dehydration catalysts [13,18]. In most cases, the two catalysts are simply physically mixed together [19–21]. However, the interest of several researchers for bifunctional catalysts, in which the two phases are in an intimate contact, is recently growing and several cases of actual bifunctional catalysts have been reported [22,23]. In this context, it is believed that the close proximity of the two type of active sites (redox and acid) would improve the performances of the catalyst, due to a more prompt dehydration of the formed methanol [1,13].

As previously mentioned, improvement in efficiency of the dehydration catalysts strongly depends on the optimization of their acidic properties, in terms of amount, typology (Brønsted or Lewis), and strength of acid sites. In this work, mesostructured γ-Al_2O_3 and three mesostructured aluminosilicates with the same Si/Al ratio (= 15) and different textural properties have been synthesized with the aim of investigating how surface acidity can be tuned by modifying the textural features rather than the Si/Al ratio of the catalysts. The different synthesized catalysts have been characterized in particular for their acid sites, by using adsorption calorimetry and Fourier-Transform Infrared (FTIR) spectroscopy using NH_3 and pyridine as probe molecule, respectively. These characterization techniques gave information about the amount, typology, and strength of the acid sites of the catalysts, allowing to correlate them with the textural properties. The catalysts have been subsequently tested to assess their catalytic performances for methanol dehydration to DME.

2. Experimental section

2.1. Chemicals

The following chemicals were used without further purification: PEG_{20}-PPG_{70}-PEG_{20} (Pluronic P-123) average Mn ~ 5800 (Aldrich Chemistry), Tetraethyl orthosilicate (TEOS) 98 % (Aldrich Chemistry), aluminum chloride hexahydrate ($AlCl_3{\cdot}6H_2O$) 99 % (Alfa Aesar), aluminum isopropoxide > 98 % (Alfa Aesar), aluminum nitrate nonahydrate ($Al(NO_3)_3{\cdot}9H_2O$) > 98 % (VWR BDH Chemicals), Nitric acid (HNO_3) ≥ 65 % (Honeywell Fluka), hexadecyltrimethylammonium bromide (CTAB) > 98 % (Sigma), ammonia solution (NH_3) 28.0–30.0 % (Sigma-Aldrich), hydrochloric acid (HCl) 37 % (VWR BDH Chemicals), sodium chloride (NaCl) 99 % (Sigma-Aldrich), and absolute ethanol (CH_3CH_2OH) (Honeywell Fluka).

2.2. Synthesis of Al-MCM-41

The procedure reported by Cara et al. [15], which was adapted from [24], was followed to synthesize the aluminum-doped MCM-41 (Al-MCM-41) with a Si/Al ratio of 15. 0.2314 g of Al(O-*i*-Pr)$_3$ were dissolved in 3.79 mL of TEOS. Within a flask, a solution of 1 g of CTAB (templating agent) in 200 g of bi-distilled water was stirred (300 RPM) at 30 °C for 3.5 h. Then, absolute ethanol (69.1 g) was added, keeping the stirring for additional 20 min. 21 mL of liquor ammonia were then poured into the flask with a successive increase in the stirring to 600 RPM. The solution of precursors was immediately added under stirring at 600 RPM, which was kept for other 5 min, resulting in a milky white dispersion. The reaction was carried out for 19 h after decreasing the stirring to 300 RPM. The as-obtained solid was subsequently washed with a 1/1 V/V water/ethanol solution and centrifuged at 4500 RPM for 10 min for three times, and dried. A calcination at 550 °C with a ramp of 5 °C/min was carried out to remove the templating agent.

2.3. Synthesis of Al-SBA-16

Al-SBA-16 was prepared by adapting the procedure from Wang et al. [25] for the synthesis of Al-SBA-15. The adoption of a Si/Al ratio (= 15), not reported in the original work, led to a cubic SBA-material (SBA-16) instead of the hexagonal counterpart. Namely, to obtain ≈ 1.5 g of product, a P123 solution was prepared into a round-bottom flask by dissolving 2.36 g of the three-block copolymer into 45 mL of absolute ethanol under continuous stirring at room temperature (RT), followed by the addition of 5.34 g of TEOS, 0.38 g of $AlCl_3{\cdot}6H_2O$, and 0.5 mL of water after 2 h. The stirring was kept for 24 h. Then, the solution was poured into a Petri dish (Ø = 21 cm) and moved into a controlled-humidity chamber (relative humidity (RH) of 40 % at RT). The 48 h-aged gel was calcined at 600 °C (2 °C/min) for 5 h.

2.4. Synthesis of Al-SBA-15

The solvothermal procedure proposed by Meloni et al. [26,27] was adopted for the synthesis of Al-SBA-15. A solution of 4 g of P123 and 6.7 g of NaCl into 126 mL of 1 M HCl was obtained under stirring at 40 °C. 8.5 g of TEOS were then poured dropwise, and the solution was stirred at 40 °C for 24 h. 1.02 g of $Al(NO_3)_3{\cdot}9H_2O$ were subsequently added and the mixture was first stirred for 24 h, then transferred into a 300 mL autoclave, and heated at 100 °C in an oven for 48 h. After this hydrothermal treatment, the pH was adjusted to 5 by the addition of concentrated ammonia (28–30 %). After that, the autoclave was sealed again and subjected to a second hydrothermal treatment at 100 °C for

48 h. Eventually, the obtained solid was separated by centrifugation (4500 RPM, 10 min), washed twice with distilled water, and dried overnight at 60 °C. A calcination step was carried out at 600 °C (4 °C/min) for 5 h.

2.5. Synthesis of γ-Al_2O_3

γ-Al_2O_3 synthesis was based on the procedure presented by Yuan et al. [28], adapted for the specific purpose, using an EISA approach with Pluronic P123 as structure directing agent. To get 1.5 g of meso-structured γ-Al_2O_3, a solution of 3 g of P123 in 75 mL of absolute ethanol was obtained into a flask under continuous stirring at RT. After ≈ 2 h, HNO_3 (4.8 mL) and aluminum isopropoxide (6.24 g) were added. The resulting solution was continuously stirred for 1 day at RT, and then poured into a Petri dish (Ø = 21 cm), which was kept into a humidity chamber with RH≈ 20% and heated on a heating plate set at 70 °C. After 2 days the sample was calcined at 900 °C (1 °C/min) for 2 h.

2.6. Characterization techniques

Small-angle X-ray diffraction patterns (SA-XRD, 2θ = 0.7–6°) were measured on a Seifert X3000 instrument with a θ–θ geometry, equipped with a Cu anode (Kα radiation of 1.5418 Å), whereas the wide-angle XRD patterns (WA-XRD) in the 2θ range between 10° and 80°) were recorded using a PANalytical X′pert Pro (Malvern PANalytical, Malvern, UK) with a copper X-ray source. The lattice parameter of the meso-structures was calculated using the equations $a_0 = \frac{2d_{100}}{\sqrt{3}}$ and $a_0 = d_{110}\sqrt{2}$ for the samples featuring a hexagonal structure (Al-MCM-41, Al-SBA-15 and γ-Al_2O_3) [24,29], and a cubic one (Al-SBA-16) [30,31], respectively. The Rietveld method was applied on the γ-Al_2O_3 XRD pattern using the software MAUD [32]. The standard reference LaB_6 from NIST was used for determining the instrumental broadening. The CIF for γ-Al_2O_3 structure (#1200015) was downloaded from Crystallography Open Database [33].

The textural properties were studied by nitrogen adsorption–desorption isotherms at − 196 °C, measured on a Micromeritics ASAP 2020 system. All samples were pre-heated under vacuum at 250 °C (heating rate, 1 °C/min) for 12 h. The Brunauer–Emmett–Teller (BET) specific surface area (SA) was determined from the adsorption data in the 0.05–0.25 P/P_0 range for all samples but Al-MCM-41 (0.05–0.17 P/P_0 range). The total pore volume (V_p) was calculated at P/P_0 = 0.9975, and the Barrett–Joyner–Halenda (BJH) model was applied to the desorption branch isotherm to determine the mean pore diameter (D_p) for all samples but Al-SBA-16 for which the adsorption branch was used instead [31]. The pore wall thickness (T_w) was calculated as the difference $T_w = a_0 - D_p$ or $T_w = a_0\frac{\sqrt{3}}{2} - D_p$ for the samples with a hexagonal meso-order or a cubic one, respectively [34,35].

A JEOL JEM 1400-PLUS microscope operating at 120 kV and a field emission gun FEI TALOS F200S microscope at 200 kV were used to obtain the transmission electron microscopy (TEM) micrographs. Chemical analyses were obtained by EDS. The samples' fine powders were dispersed in ethanol, sonicated, and the resulting suspensions dropped onto 200 mesh carbon-coated copper TEM grids.

To determine the nature of the acid sites, Fourier Transform Infrared spectroscopy (FT-IR) analyses were carried out using pyridine as a probe molecule (Py-FTIR). FT-IR spectra were recorded using a Nicolet iS50 spectrometer manufactured by Thermo Fischer Scientific and equipped with a custom-made glass cell; inside the cell, the sample can be moved between two different positions allowing to either heat the sample or acquiring the spectrum. The cell was evacuated ($< 1.3\cdot10^{-3}$ Pa) by a rotative pump and a turbomolecular pump. Details on the experimental setup were provided in a previous work [15]. The FT-IR spectra were acquired between 1700 cm^{-1} and 1400 cm^{-1}. Circular self-supported pellets with a diameter of 13 mm were prepared for each sample before the analysis; particularly, 15–20 mg of sample were pressed for 2–3 min at 2500–3000 kg with a hydraulic press. The as-obtained pellet was then inserted into the cell and subjected to a thermal treatment at 250 °C (7.5 °C/min) for 1 h under high vacuum in order to ensure a complete desorption of the water molecules. The sample, continuously kept under high vacuum, was subsequently moved in the measurement position, let to cool down to room temperature, and its spectrum was acquired as a background. The sample was then saturated with pyridine, allowing the cell to reach a pressure of about 267 Pa with pyridine vapor and keeping these conditions for 10 min. The cell was then again evacuated at RT, and the spectrum acquired. The analysis was repeated after heating the sample at various temperatures (100 °C, 200 °C, 300 °C) under high vacuum; after each treatment, the sample was let to cool down to room temperature before acquiring the spectrum. These thermal treatments at increasing values of temperature allowed to study the progressive desorption of pyridine from the acid sites of the sample. The area under the IR signals associated with each type of acid sites was estimated to quantify the number of acid sites still occupied by pyridine at each temperature. Specifically, the band at about 1455 cm^{-1} was used to estimate the number of Lewis acid sites, using an Integrated Molar Extinction Coefficient (IMEC) of 2.22 cm/μmol; whereas the band at about 1545 cm^{-1} was used for the Brønsted acid sites, with an IMEC of 1.67 cm/μmol [36].

The microcalorimetric measurements were conducted by a Tian-Calvet heat flow calorimeter (Setaram) equipped with a volumetric vacuum line. About 100 mg of the sample were treated overnight at 300 °C under vacuum (1 Pa) prior to the introduction of small doses of ammonia, *i.e.* the probe gas. The equilibrium pressure associated with each adsorbed amount was measured by a differential pressure gauge (Datametrics) and the thermal effect recorded. The run was stopped at a final equilibrium pressure of ca. 133 Pa. The adsorption temperature was kept at 80 °C to avoid physisorption. The run was repeated after overnight outgassing at 80 °C. The adsorption and calorimetric isotherms were acquired for each run. The adsorption isotherms allow the correlation between the amount of probe gas and the corresponding equilibrium pressure. The overall ammonia uptake was assessed from the first isotherm ($n_{A,tot}$). The amount of the irreversibly adsorbed ammonia ($n_{A,irr}$) was calculated by subtracting the second isotherm, obtained after outgassing the sample, from the first one. The calorimetric isotherms provide the relationship between the integral heat of adsorption and the corresponding equilibrium pressure. A plot of the differential heat of adsorption as a function of the adsorbed amount was obtained by combining the adsorption and calorimetric data, revealing information on the influence of the surface coverage on the energetics of the adsorption. A differential heat (Q_{diff}) cut-off value between specific and non-specific (physisorption) adsorbent/adsorbate interactions was fixed to 70 kJ/mol, based on adsorption experiments on an Al-free silica sample [27]. However, this value corresponds for the Al-SBA-15 to a final plateau, ascribable to the presence of sites with Q_{diff} that differ by less than 5 kJ/mol. Considering that these might be reasonably considered as isoenergetic sites, which would be excluded assuming 70 kJ/mol as the cut-off, a Q_{diff} of 75 kJ/mol was used instead to calculate the amount of total acid sites for this sample.

2.7. Catalytic tests

A customized Microactivity Effi (PID Eng&Tech) bench-scale plant, employing a high-pressure fixed-bed stainless steel reactor (length 304.8 mm, inner diameter 9.1 mm), was used for the DME production experiments. The catalytic bed was supported inside the isothermal zone of the reactor by a porous plate (made of Hastelloy C, 20 μm) and quartz wool. The dehydration catalysts were tested in form of physical mixtures with a commercial Cu-based redox catalyst (CZA). Particularly, both CZA and the dehydration catalysts were first separately ground into an agate mortar to obtain fine powders, then 50 mg of redox phase (CZA), 200 mg of acidic catalyst, and 3.2 g of α-Al_2O_3, a chemically inert material were physically mixed using a steel spatula inside a Teflon

weighing boat. A total bed volume of ca. 3 cm^3 was thus obtained and, as a result, under a constant inlet flow rate, the gas hourly space velocity (GHSV) was 48,000 N cm^3 g_{cat}^{-1} h^{-1}.

Firstly, all fresh catalysts were in-situ reduced under a H_2/N_2 gas mixture (H_2, 15 vol% in N_2) at 250 °C for 2 h under atmospheric pressure. Then, at the same temperature, a gaseous stream made up of a 3:1 (molar ratio) mixture of H_2 and CO_2 and 10 vol% of N_2 (internal standard for gas chromatographic analysis) was fed and the pressure was allowed to reach 3.0 MPa. Once the system reached the steady state in 1 h on stream, analyzes were performed repeatedly on the reaction stream during the run, conducted for 36 h. The analyzes were performed with a 7890B (Agilent) gas chromatograph equipped with a flame ionized detector (FID) and a thermal conductivity detector (TCD) for carbon-containing compounds and for permanent gases, respectively. The components of the outlet gas mixture were separated by two columns connected in series: CO_2, CH_3OH, DME, CH_3CH_3, and $CH_3CH_2CH_3$ were separated by a HP-PLOT Q (Agilent) column (length 30 m, inner diameter 0.53 mm, film thickness 40 μm), while a HP-PLOT Molesieve (Agilent) column (length 30 m, inner diameter 0.53 mm, film thickness 50 μm) allowed the separation of H_2, N_2, CH_4, and CO. To avoid condensation of products, the pipelines connecting the plant gas outlet to the gas chromatograph inlet were heated at 180 °C. The CO_2 conversion (X_{CO2}) and the products selectivity (S_P, with P: CH_3OH, DME, or CO), were calculated by the following equations:

$$X_{CO_2} = \frac{n_{CO_2}^{in} - n_{CO_2}^{out}}{n_{CO_2}^{in}} \times 100$$

$$S_P = \frac{\nu_{CO_2}}{\nu_P} \times \frac{n_P^{out}}{n_{CO_2}^{in} - n_{CO_2}^{out}} \times 100$$

where n_i^{in} and n_i^{out} are the moles of the i-th species in the inlet and outlet stream respectively, and ν_i is the stoichiometric coefficient of the i-th species in the balanced equation.

In order to estimate the standard deviation for conversion and selectivity (2–5 %), a catalytic run on a commercial catalyst was repeated three times [37].

3. Results and discussion

3.1. Mesostructured acidic catalysts: structural and textural characterization

Fig. 1a reports the small-angle X-ray diffraction (SA-XRD) of the mesostructured acidic catalysts. SA-XRD patterns show the presence of mesoporous order for all samples, clearly indicated by the presence of peaks, with substantial differences among the samples. Al-SBA-15, obtained with the solvothermal sol-gel method, exhibits a hexagonal mesostructure, indicated by the main peak (100) located at very low (0.9°) 2θ values, and two low-intensity peaks (110; 200) located at 1.5° and 1.8°, respectively. A cell parameter of 10.8 nm was calculated (Table 1). Al-SBA-16, prepared with an EISA approach, shows a main peak (110) located at a 2θ value of 1.2°, associated with a cell parameter of 10.6 nm; the pattern also shows a peak (200) located at 1.3°. The presence of these peaks indicates a cubic SBA-16-like pore arrangement (*Im3m*) [35,38]. A mesostructure with a significantly smaller cell parameter (3.9 nm), and consequently smaller pores, was showed by Al-MCM-41, as indicated by a broad peak located at about 2.6°. In this case, the pore arrangement geometry could not be clearly attributed, due to the lack of additional signals besides the main peak; however, a hexagonal arrangement was assumed on the basis of the synthesis conditions selected that, in absence of aluminum, lead to a hexagonal mesostructure (MCM-41) [24]. γ-Al_2O_3 X-ray pattern shows a 100 peak located at about 1.1°, attributable to a hexagonal cell parameter of 9.3 nm; the broad band present at about 1.9°, where the 110 and 200 peaks are located, suggests the formation of a hexagonal mesostructure with a relatively low degree of mesoporous order. The position of the bands is in agreement with the data presented in the literature for γ-Al_2O_3 with a hexagonal mesoporous structure [28,39,40].

Fig. 1b depicts the wide-angle X-ray diffraction patterns (WA-XRD) of the four mesostructured samples. As expected, all aluminosilicate systems proved to be amorphous, showing a main broad band located at a 2θ value of about 23°, attributed to amorphous silica. The alumina sample, on the other hand, clearly shows broad diffraction peaks attributed to cubic γ-Al_2O_3 phase in form of small nanoparticles (PDF card 00-047-1292). The Rietveld refinement (Fig. S1) performed on the pattern pointed out a mean crystallite size of 5.1(1) nm with a microstrain of $2.3(1)\cdot10^{-3}$, indicating about 2 defects out of 10^3 lattice planes. The calculated cell parameter, 7.879(4) Å, is slightly smaller than the one reported in the literature (7.9448 Å, PDF card 00-047-1292). The refinement also permits to visualize two broad bands at about 36° and 63°, close to the main reflections of aluminum oxide, associated with a

Table 1
BET surface area (SA), pore volume (V_p), cell parameter (a_0), mean BJH pore diameter (D_p) and wall thickness (T_w) of the samples.

Sample	SA (m^2/g)	V_p (cm^3/g)	a_0 (nm)	D_p (nm)	T_w (nm)
Al-MCM-41	1262	0.77	3.9	2.1 ± 0.7	1.7
Al-SBA-16	437	0.52	10.6	4.6 ± 0.5	4.6
Al-SBA-15	673	1.07	10.8	6.9 ± 0.5	3.8
γ-Al_2O_3	197	0.57	9.3	5.6 ± 1.7	3.9

Relative standard deviation: %RSD (SA) = 2.1 %; %RSD (V_p) = 1.1 %; %RSD (D_p) = 1.8 %.

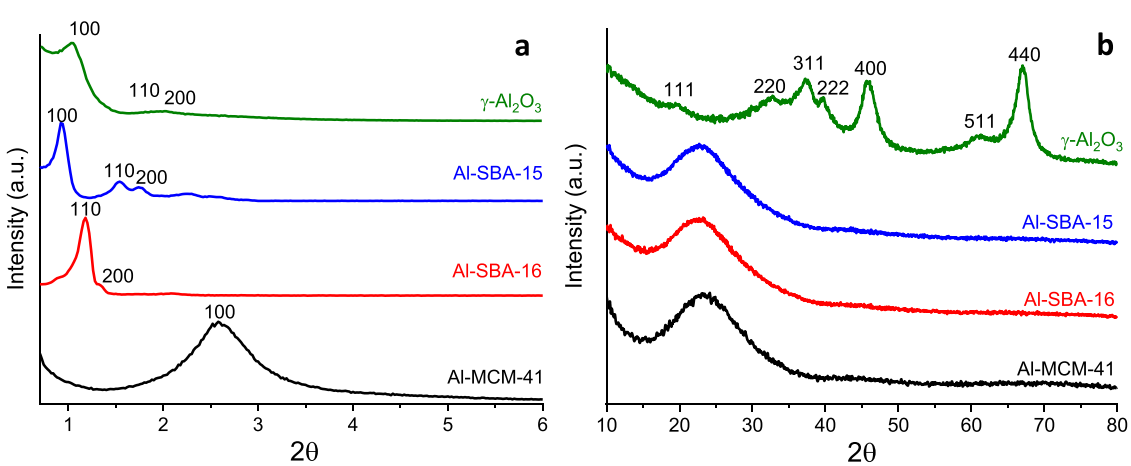

Fig. 1. Small-angle (a) and wide-angle (b) X-ray diffraction patterns of the samples.

small amount of amorphous alumina still present after the thermal treatment.

Nitrogen physisorption measurements confirmed the mesoporous nature of all samples (Fig. 2a), pointed out by the shape of the isotherms, featuring a capillary condensation branch for all samples; furthermore, for all aluminosilicates, it can be observed that multilayer adsorption is preceded by a microporous contribution. As expected, the capillary condensation branch of Al-MCM-41 sample (type IVb isotherm) is located at the lowest value of relative pressure (< 0.3) among all samples, indicating a smaller mean pore diameter (2.1 nm). Al-SBA samples show isotherms (type IVa) featured by hysteresis cycles with steeper capillary condensation branches located at higher values of relative pressure, namely 0.5–0.6 for Al-SBA-16 and 0.7–0.8 for Al-SBA-15, indicating pore diameter values significantly larger than those of Al-MCM-41, confirming the results showed by SA-XRD patterns; the two Al-SBA samples, however, showed different hysteresis cycles. Al-SBA-15, particularly, showed a narrow hysteresis cycle with very steep and perpendicular adsorption and desorption branches (type H1, according to IUPAC classification), indicating a narrow pore size distribution and a well-defined arrangement of cylindrical pore channels [26,41]; Al-SBA-16, on the other hand, showed a less steep adsorption branch (H2 hysteresis type according to IUPAC), usually shown by SBA-16 materials [30,35,42]. γ-Al_2O_3 sample shows isotherms featured by a capillary condensation branch, indicating the presence of mesopores; the hysteresis branches, in this case, are much less steep than those showed by Al-SBA samples, indicating the presence of a mesoporous order of lower degree [43–45]. As regards the textural properties of the samples (Table 1), Al-SBA-15 showed the highest pore volume (1.07 cm^3/g) and pore diameter (6.9 nm) among all the samples; Al-MCM-41, on the other hand, showed the highest BET surface area (1262 m^2/g), associated with the lowest pore diameter (2.1 nm).

The pore size distribution calculated with BJH method (Fig. 2b) shows a narrow pore size distribution for all the aluminosilicate samples. Al-MCM-41, Al-SBA-16 and Al-SBA-15 feature a mean pore size of 2.1 ± 0.7 nm, 4.6 ± 0.5 nm, and 6.9 ± 0.5 nm respectively. The pore distribution curve of γ-Al_2O_3 (mean pore size 5.6 ± 1.7 nm), on the other hand, was much lower and wider, indicating a lower degree of porous order, as already observed from the isotherms.

TEM micrographs prove the presence of an ordered mesoporous structure for all samples (Fig. 3). Al-MCM-41 was obtained in form of spherical particles (Fig. 3a-c) with a mean diameter of about 250 ± 20 nm (Fig. S2) and showed the smallest pore diameter (Fig. 3d). TEM micrographs of Al-SBA-15, Al-SBA-16, and γ-Al_2O_3 show an ordered pore structure with a significantly higher pore diameter than that showed by Al-MCM-41, as expected. Al-SBA-16 shows the presence of a cubic mesopore arrangement, as can be clearly seen by the perpendicular view of the pore channels (Fig. 3e–h). Aware of the intrinsic limit of electron microscopy in transmission mode in determining pore size, due to the thickness of the sample, that leads to an underestimation of the pore size and, consequently to an overestimation of the wall thickness, mean pore diameter was nevertheless estimated for all samples, aside Al-MCM-41. The pore diameter estimated by TEM micrographs (Fig. 3h) shows a narrow distribution (3.0 ± 0.3 nm), and a lower mean diameter than that calculated with BJH method (4.6 nm); this fact, besides the intrinsic limit mentioned above, can be explained considering that the SBA-16 structure features a cubic pore arrangement with large cages interconnected by smaller channel pores. Since the cages are hidden by the pore walls and only the interconnecting channels are visible, the pore size estimation from TEM micrographs gives a lower pore diameter as result. Some TEM micrographs (Fig. 3h), due to the low thickness of the sample in that zone, clearly show the presence of the cages interconnected by pore channels; the size of the cages estimated from TEM micrographs is (5.2 ± 0.4 nm). The value of wall thickness determined from TEM micrographs is 4.5 ± 0.5 nm, in very good agreement with the data obtained from the cell parameter and BHJ pore diameter (4.6 nm). Al-SBA-15, on the other hand, clearly shows the presence of an ordered mesoporous structure with a hexagonal arrangement (Fig. 3i–l), confirmed by the observation of a honeycomb-like structure as well as a parallel arrangement of the channels; Al-SBA-15 also exhibits the highest pore diameter (6.7 ± 0.8 nm) among all samples, as already confirmed by the data obtained from nitrogen physisorption; this value, together with an associated wall thickness of 4.1 ± 0.5 nm is in agreement with the data obtained from nitrogen physisorption (D_p = 6.9 nm, T_w = 3.8 nm) reported in Table 1; the slight underestimation can be ascribed to the intrinsic limit of TEM microscopy mentioned above and, for a hexagonal geometry, to the fact that the optimal alignment of the electron beam with the C_6 axis of symmetry is rarely achieved [46]. γ-Al_2O_3 also shows a hexagonal mesoporous structure (Fig. 3m-p); however, the degree of mesoporous order, was much lower than that showed by Al-SBA-15, as the sample exhibits some areas with a disordered mesoporosity (Fig. 3m, see arrows). This finding confirmed what was previously observed from nitrogen physisorption; TEM micrographs also pointed out the presence of large interparticle cavities (Fig. 3n, see arrows). The mean pore size determined from TEM micrographs for γ-Al_2O_3 is 5.0 ± 0.5 nm with a wall thickness of 4.1 ± 0.5 nm, very close to the value calculated with BJH method (D_p = 5.6 nm, Table 1) and from its difference with the cell parameter (T_w = 3.9 nm, Table 1). The calculated wall thickness is in good agreement with Rietveld refinement results, indicating, a crystallite size of about 5 nm.

EDX chemical mapping (Fig. 4), performed on all three aluminosilicate samples, reveals a homogeneous distribution of Si and Al atomic

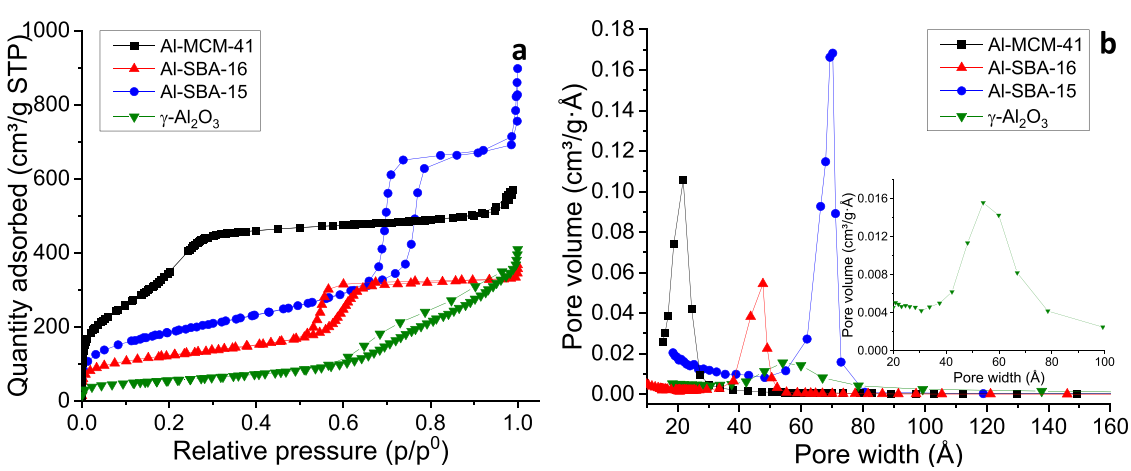

Fig. 2. Nitrogen physisorption isotherms (a) and BJH pore size distribution (b) for all samples. The inset in (b) depicts BJH pore size distribution of γ-Al_2O_3.

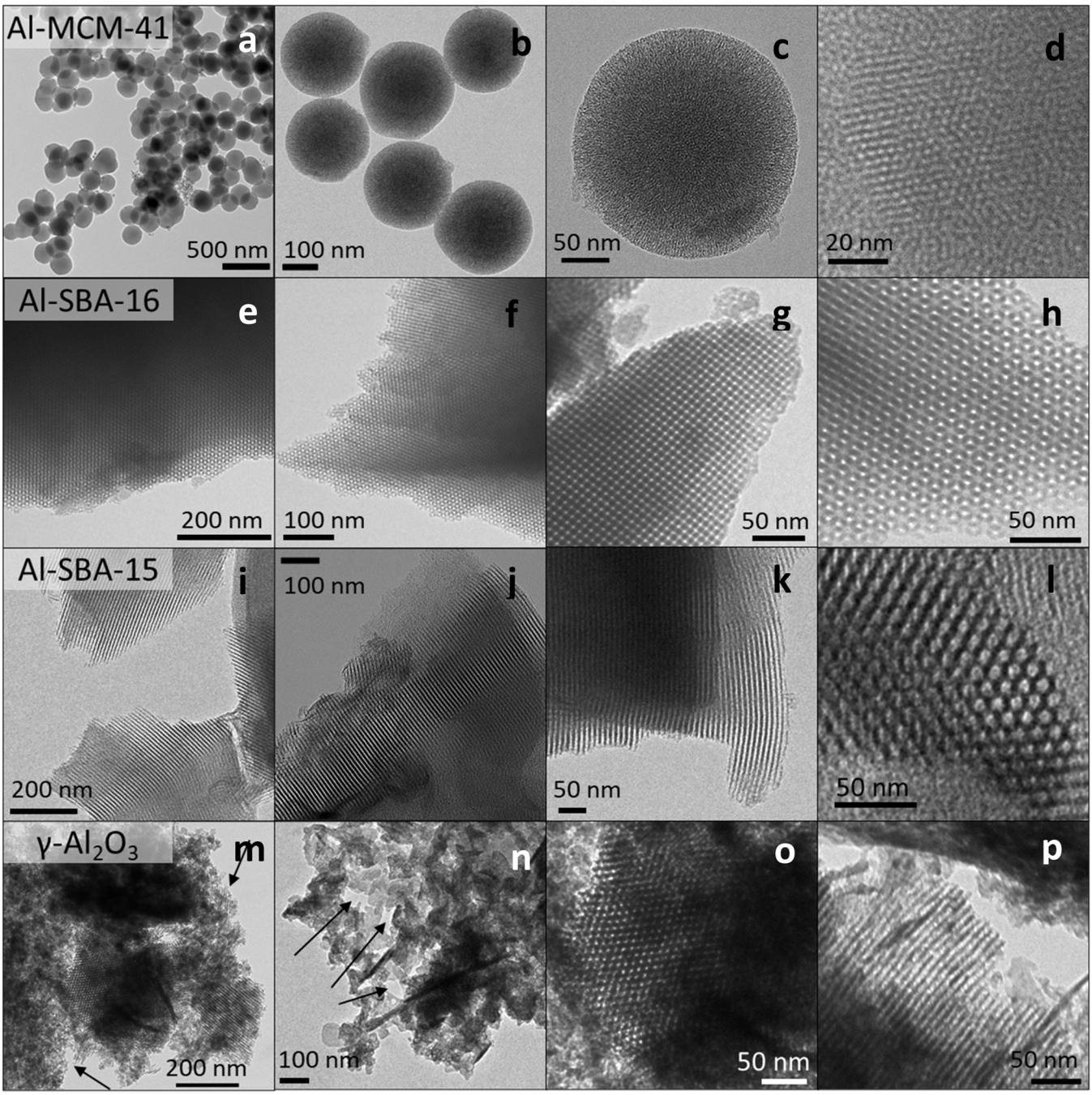

Fig. 3. TEM images of Al-MCM-41 (a–d), Al-SBA-16 (e–h), Al-SBA-15 (i–l), and γ-Al_2O_3 (m–p).

species throughout the samples. Semi-quantitative analysis performed by EDX points out a Si/Al ratio of 15 ± 1 for all samples, confirming the theoretical ratio used in the synthesis processes.

3.2. Mesostructured acidic catalysts: acid sites characterization

All the mesostructured systems presented in this work were subjected to characterization of the acid sites with FT-IR spectroscopy using pyridine as probe molecule (Py-FTIR). This technique allows the quantitative estimation of the amount of both Lewis and Brønsted acid sites, according to different bands in the FTIR spectra, acquired after outgassing at various temperatures, ranging from 25 to 300 °C, after the saturation of the sample with pyridine. In the literature FTIR spectroscopy with a probe molecule is a widely used characterization technique that allows to assess the typology of the acid sites present in the investigated samples; however, quantification, despite being possible, is not always performed [47]. Furthermore, the few systematic works usually focus on the investigation of the same type of material (*e.g.* Al-SBA-15 [41,47–49] or Al-MCM-41 [50]) with different Si/Al ratios or on the comparison of very different materials as amorphous *vs* crystalline aluminosilicates (zeolites) *vs* γ-Al_2O_3 [49,51,52]. In this work, our goal is to study how the acidity of three amorphous mesostructured aluminosilicates, synthesized with the same Si/Al ratio, is affected by their different textural properties (pore order, pore size, surface area, and pore volume) and to compare their acidic properties with those of a mesostructured γ-Al_2O_3. In agreement with what previously observed for Al-MCM-41 [15] and with the data reported in the literature for Al-SBA-15 samples [47,48,53], all three aluminosilicate samples show the presence of

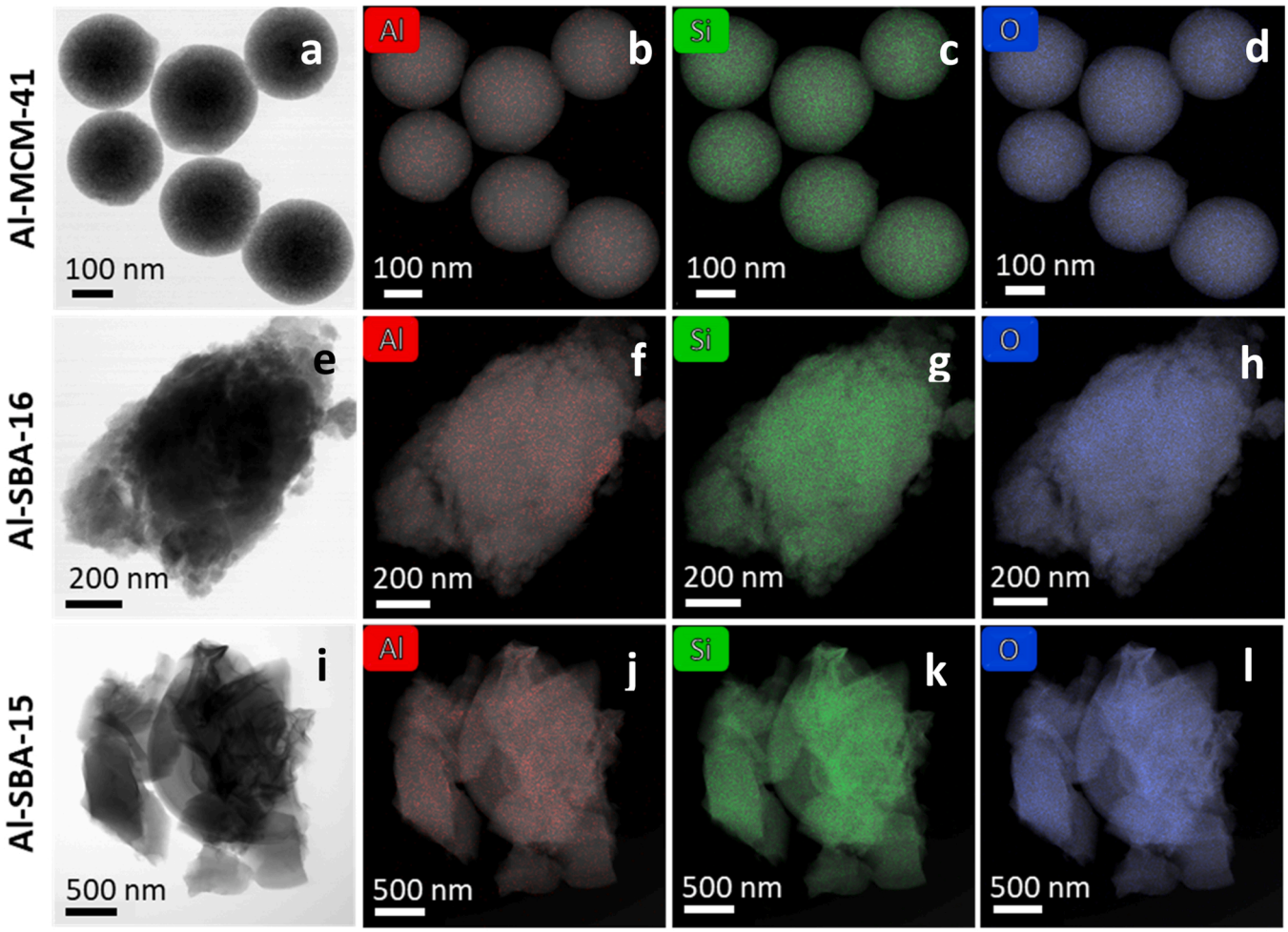

Fig. 4. EDX chemical mapping of Al-MCM-41 (a–d), Al-SBA-16 (e–h), and Al-SBA-15 (i–l).

both Lewis and Brønsted acid sites (Figs. 5a–c and 6a–c). The spectra acquired at room temperature also point out the presence of pyridine physically adsorbed on silanol groups (H-bond); however, these signals disappear at 100 °C, indicating the weak nature of this kind of interactions. As expected, increasing the temperature from 25 to 300 °C, a gradual decrease in the intensity of the signals associated to both Lewis and Brønsted acid sites can be observed for all samples (Fig. 6a–c; Tables S1–S3); this trend clearly indicates a progressive desorption of pyridine from both types of acid sites. The desorption of pyridine associated with the temperature increase is much more prominent for Brønsted sites, as can be clearly seen also from the Brønsted/Lewis ratio (Figs. 6a–c and 7a; Tables S1–S3) that progressively decreases, clearly suggesting that Lewis sites are remarkably stronger than Brønsted ones. This fact is in agreement with previous studies on samples that feature only the presence of Lewis sites, which are prone to deactivation due to water adsorption [13,14]. Brønsted sites, on the other hand, besides their different nature, which does not allow the formation of a Lewis adduct, are less sensitive to the presence of water, being their interaction with water weaker than that showed by Lewis sites, and thus ideal sites for methanol dehydration catalysts. The progressive decrease of Brønsted/Lewis ratio with an increase in temperature was also observed by Occelli et al. [50], who, however, found that not all investigated samples showed that trend, as it really depends on the synthesis method and the precursors used. An opposite trend of the Brønsted/Lewis sites ratio along with increasing temperature was instead observed by other authors for Al-SBA-15 [48]. In the present work, for all investigated temperatures, the value of Brønsted/Lewis ratio increases in the order Al-SBA-16 > Al-SBA-15 > Al-MCM-41 (Fig. 7a; Tables S1–S3); the same trend is also shown by the total amount of acid sites (Brønsted + Lewis) expressed in terms of μmol/m^2 (Tables S1–S3).

An inverse behavior is observed for the total amount of acid sites in terms of μmol/g at room temperature, namely Al-MCM-41 (210 μmol/g) > Al-SBA-15 (164 μmol/g) > Al-SBA-16 (143 μmol/g). However, this trend is almost exclusively ascribed to the decrease in the number of Lewis sites from 108 μmol/g (for Al-MCM-41) to 72 μmol/g (for Al-SBA-15) to 55 μmol/g (for Al-SBA-16), being the amount of Brønsted sites almost constant (94 ± 7 μmol/g). This fact suggests that, for the same Si/Al ratio, the remarkable difference in textural properties mainly affects the amount of Lewis sites, having little effect on Brønsted sites. This trend is also observed at 100 °C, where the contribution of physisorbed pyridine is excluded; at this temperature, the amount of Brønsted sites is almost constant (84 ± 7 μmol/g) while the number of Lewis sites decreases from 85 μmol/g (Al-MCM-41) to 53 μmol/g (Al-SBA-16). At higher temperatures, the aluminosilicates still do not show remarkable differences in the amount of Brønsted sites. Furthermore, from the data gathered from FTIR of pyridine after desorption at various temperature, it can be inferred that Brønsted sites on the different samples feature similar strengths.

As for γ-Al_2O_3 sample, FTIR spectra only show bands attributable to Lewis acid sites (Fig. 5d), in agreement with what have been observed by other authors in the literature [54–56]; however, in this case, it has to be pointed out how the main band attributed to Lewis sites gradually shifts from 1448 cm^{-1} to 1453 cm^{-1} while increasing the desorption temperature from 25 °C to 300 °C. This fact can be attributed to the desorption of pyridine from either weak Lewis sites or surface hydroxyl groups. A similar shift is also observable for the Lewis band located at

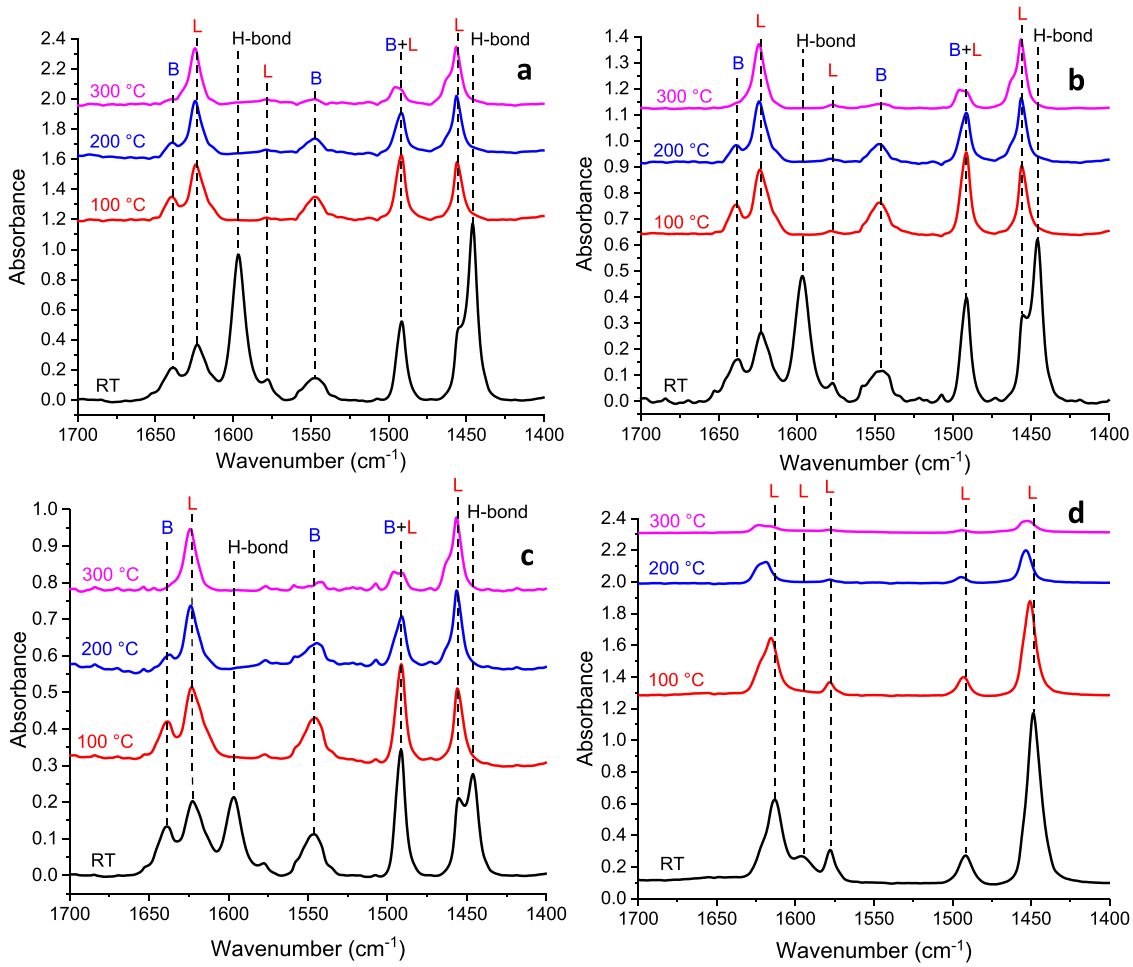

Fig. 5. FTIR spectra of adsorbed pyridine for Al-MCM-41 (a), Al-SBA-15 (b), Al-SBA-16 (c), and γ-Al_2O_3 (d).

1613 cm^{-1} at RT, associated with the disappearance of the band at 1596 cm^{-1}, attributed either to H-bonded pyridine [57] or weak Lewis sites [55] by different authors. With this is mind, it must be pointed out that the amount of Lewis sites at RT is presumably overestimated. The quantitative characterization on this sample after desorption at various temperatures highlights an important aspect. The Lewis sites present on γ-Al_2O_3, indeed, show a much more remarkable decrease of their number with the increase in temperature (Fig. 6; Table S4) than that shown by aluminosilicates; this finding indicates that the Lewis sites on γ-Al_2O_3 are much weaker than those present on the aluminosilicates, in agreement with what reported in the literature [49].

The acidic properties of the samples were also studied using ammonia adsorption microcalorimetry, a technique widely reported for the investigation of acidic samples such as aluminosilicates and γ-Al_2O_3 [27,58–60]. The results (Fig. 8; Fig. S3; Table S5) point out similar amounts of acid sites on all aluminosilicates, namely 420, 446, and 422 μmol/g for Al-MCM-41, Al-SBA-15, and Al-SBA-16, respectively, which can reasonably be ascribed to the same Si/Al ratio (= 15) of the three samples. Interestingly, the amount of acid sites on which ammonia is irreversibly adsorbed at 80 °C shows the same trend (Al-MCM-41 > Al-SBA-15 > Al-SBA-16, see Fig. 8a) observed for the total amount of acid sites (Brønsted + Lewis) gathered from Py-FTIR at 100 °C. Considering that Lewis sites are significantly stronger than Brønsted sites, as evidenced from FTIR measurements, the higher amount of irreversible acid sites on Al-MCM-41 and Al-SBA-15 can then be attributed to their higher number of Lewis sites. Accordingly, among the three aluminosilicate samples, Al-MCM-41 showed the highest percentage or irreversible acid sites (68 %), and, on the other hand, the lowest percentage was shown by Al-SBA-16 (52 %), as reported in Table S5. Noteworthy, the determination of acid sites with the two different techniques (FTIR spectroscopy *vs* microcalorimetry) gives comparable results (Fig. 7b) despite the different basic strength and steric hindrance of the probe molecules (pyridine *vs* NH_3) and the different temperatures (100 °C *vs* 80 °C).

As expected, considering the remarkable differences in terms of surface areas among the three aluminosilicates, an opposite trend is shown by the surface density of total acid sites, *i.e.* the amount of acid sites expressed as μmol/m^2 (Fig. 8b; Table S5). In this case the trend Al-SBA-16 > Al-SBA-15 > Al-MCM-41 is observed, pointing out a significantly higher acid site surface density for Al-SBA-16 (0.97 μmol/m^2); this fact can be clearly attributed to the relatively low surface area of this mesostructured system. On the other hand, Al-MCM-41, the sample with the highest surface area, showed the lowest surface density of acid sites (0.33 μmol/m^2). As expected, the same trend is observed for the surface density of irreversible acid sites (Fig. 8b; Table S5).

γ-Al_2O_3 shows a significantly lower amount of both total and irreversible acid sites, confirming the assumption that its Lewis acid sites are much weaker than that present on aluminosilicate samples, as pointed out by FTIR of adsorbed pyridine. Since the calorimetric measurements are carried out at 80 °C, it can indeed be presumed that, at this temperature, a large portion of acid sites is not strong enough to adsorb ammonia. Due to its low surface area, γ-Al_2O_3 shows the highest surface density of total acid sites.

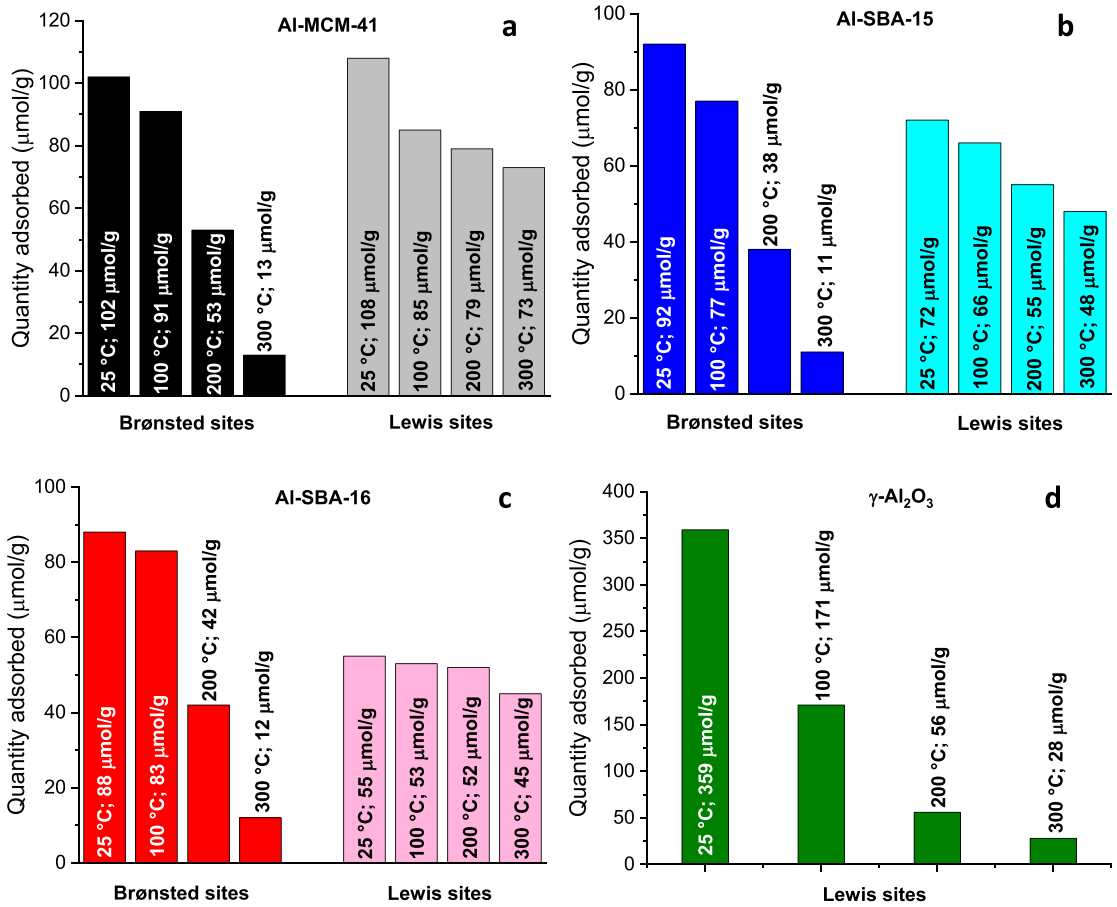

Fig. 6. Amount of Brønsted and Lewis acid sites determined with Py-FTIR on Al-MCM-41 (a), Al-SBA-15 (b), Al-SBA-16 (c), and γ-Al_2O_3 (d).

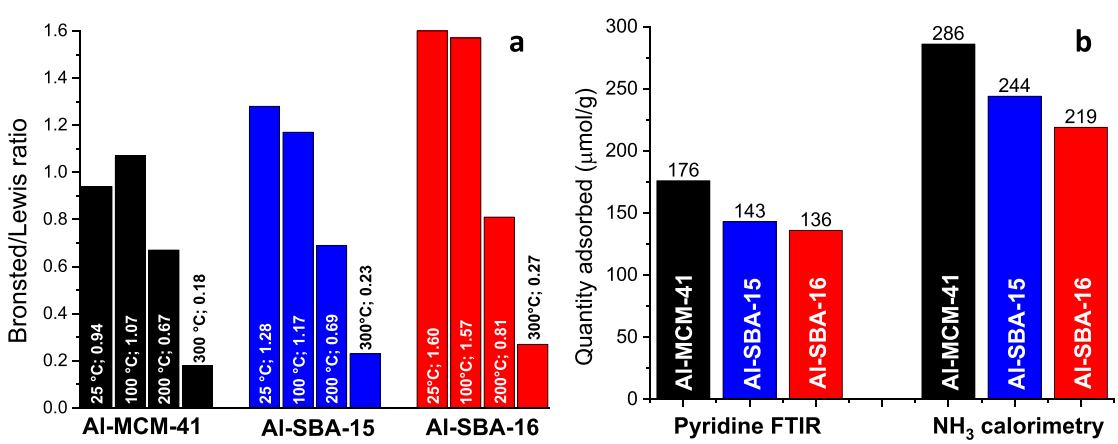

Fig. 7. Brønsted/Lewis ratio determined on aluminosilicate samples with Py-FTIR at different temperatures (a). Comparison between the amount of total acid sites determined at 100 °C on aluminosilicate samples with Py-FTIR and the amount of irreversible acid sites determined with NH_3 adsorption calorimetry (b).

3.3. Mesostructured acidic catalysts: catalytic performances

The results of the catalytic tests for methanol dehydration in the CO_2-to-DME process for all the acid catalysts in the form of physical mixtures with a commercial $CuO/ZnO/Al_2O_3$-based redox catalyst (CZA) are depicted in Fig. 9 as mean values; the catalytic performances over time are reported in Fig. S4. As can be seen from the histograms, the values of CO_2 conversion are equal within the experimental error (5 %) for all the catalysts; this can be ascribed to the fact that the redox catalyst is the main responsible for the conversion of CO_2, which is transformed into methanol through a hydrogenation reaction catalyzed by Cu. A first important difference can be noticed for the selectivity to CO, an undesired by-product deriving from the RWGS reaction. Al-SBA-16 shows a significantly lower CO selectivity (39 %) if compared with the other three catalysts (43–45 %) accompanied by the highest value of selectivity to DME (27 %), proving to be, by far, the best methanol dehydration catalyst. Consequently, it also shows the lowest value of selectivity to methanol (35 %). Al-SBA-15 and Al-MCM-41, on the other

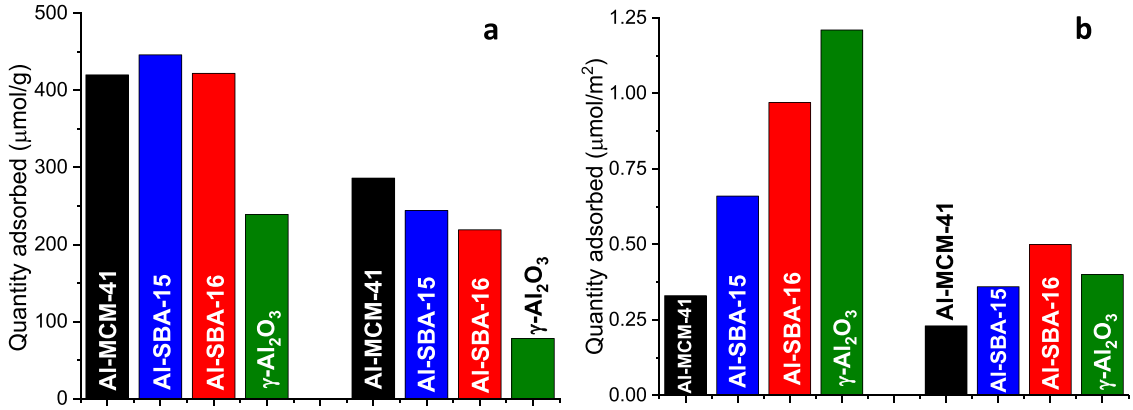

Fig. 8. Amount of total and irreversible acid sites determined with NH_3-adsorption microcalorimetry for all samples in terms of μmol/g (a) and μmol/m^2 (b).

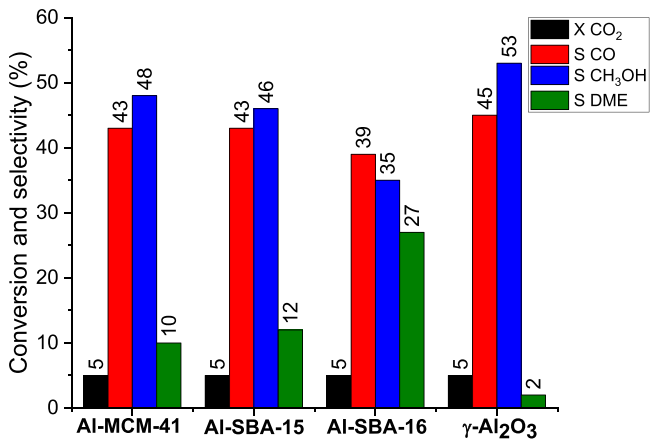

Fig. 9. Mean values of CO_2 conversion and selectivity to CO, methanol, and DME for catalytic tests on CZA-dehydration catalyst physical mixtures. Catalytic conditions: time on stream: 36 h; temperature: 250 °C; pressure: 3.0 MPa; GHSV: 48,000 N cm^3 g_{cat}^{-1} h^{-1}. Weight Ratio CZA:dehydrant = 1:4 (50 mg: 200 mg).

hand, showed significantly lower values of selectivity to DME (12 % and 10 % respectively), and higher values of selectivity to methanol, proving to be much less effective methanol dehydration catalyst than Al-SBA-16. The lowest performances are shown by γ-Al_2O_3, featuring a DME selectivity of 2 % associated with the highest methanol and CO selectivity among all catalysts (45 % and 53 % respectively).

From the analysis of the catalytic data and of the acidic properties of the dehydrating materials, it clearly emerges that there is no correlation between the dehydration activity (Al-SBA-16 >> Al-SBA-15 ≈ Al-MCM-41 >> γ-Al_2O_3) and the total amount of sites (Q_{diff} ≥ 75 kJ/mol) determined with NH_3-microcalorimetry (Fig. 8; Table S5). Furthermore, considering the overall amount of acid sites determined by Py-FTIR at 100 °C, where the contribution due to physisorbed pyridine can be excluded (Fig. 6; Tables S1–S4), it can be observed that, while this parameter increases in the order γ-Al_2O_3 ≈ Al-MCM-41 > Al-SBA-15 > Al-SBA-16, DME selectivity shows the opposite trend. In the literature, there are clear indications that dehydration activity is related to the amount and strength of Brønsted acid sites, being the Lewis sites strongly affected by deactivation due to water adsorption, as already observed in a previous work [15]. The lower activity of Lewis sites finds confirmation in the performances of γ-Al_2O_3 that, as evidenced by Py-FTIR measurements, only shows the presence of Lewis sites (Fig. 6d; Table S4). However, the dehydration activity of aluminosilicates cannot be correlated to the amount of Brønsted sites either, being their amount similar for all the three samples at all temperatures, presumably due to the same Si/Al ratio.

With this in mind, methanol dehydration performances in terms of DME selectivity, which increases in the order Al-SBA-16 >> Al-SBA-15 ≈ Al-MCM-41, could instead be associated with the surface density of acid sites. This conclusion is motivated considering that the reaction of methanol dehydration to dimethyl ether involves two molecules of methanol. The proximity between the acid sites, then, promotes methanol dehydration, allowing faster kinetics. Therefore, being Al-SBA-16 the aluminosilicate with the lowest surface area, we can infer that the maximization of the surface area, in this specific case, is detrimental for catalytic activity. The calculation of the surface density of Brønsted acid sites, reported in Table 2, determined from Py-FTIR at 100 °C, points out that the Al-SBA-16 is the sample with the highest surface density (0.19 μmol/m^2) much higher than the other two samples (0.11 μmol/m^2 for Al-SBA-15 and 0.07 μmol/m^2 for Al-MCM-41). The same trend is shown by the surface density of the sites on which ammonia is irreversibly adsorbed, determined by NH_3-microcalorimetry (Table 2). The trend of the surface density of Brønsted acid sites is also confirmed at higher temperatures (200 and 300 °C, see Tables S1–4). Accordingly, Al-SBA-16, despite having the lowest amount of total acid sites and the lowest surface area and pore volume among the three aluminosilicates, is the best methanol dehydration catalyst due to the high surface density of its Brønsted acid sites.

Additionally, the catalytic performances of aluminosilicates towards methanol dehydration might also be affected by the textural properties and mesopore arrangement, which in principle can give rise to differences in diffusion of the molecules during the reaction. Particularly, the 3D cubic porous structure of Al-SBA-16 (*Im3m*) may allow a more rapid diffusion of the molecules of reactants and products during the reaction if compared with the 2D hexagonal porous structure of Al-SBA-15 (P6mm), as already observed in the literature [61,62], further justifying the difference in terms of selectivity to DME. Similarly, comparing the two catalysts with the same hexagonal mesopore arrangement (Al-SBA-15 and Al-MCM-41), it can be reasonably assumed that the

Table 2
Correlation of the acidic features of the samples with the catalytic performances.

Sample	Py-FTIR tot. sites at 100 °C (μmol/m^2)	Py-FTIR Brønst. sites at 100 °C (μmol/m^2)	NH_3-Cal Vtot (μmol/m^2)	NH_3-Cal Virr (μmol/m^2)	S_{DME} (mol %)
Al-MCM-41	0.139	0.072	0.333	0.227	10
Al-SBA-15	0.212	0.114	0.663	0.363	12
Al-SBA-16	0.311	0.190	0.966	0.501	27
γ-Al_2O_3	0.868	-	1.21	0.40	2

larger pores of Al-SBA-15 (6.9 nm) allow a faster diffusion than the smaller ones (2.1 nm) of Al-MCM-41. However, since the molecules involved in the dehydration reaction (*i.e.* methanol and dimethyl ether) are significantly smaller than the size of the mesopores, it can be inferred that the mesopore arrangement and the pore size have a minor effect on diffusivity and, consequently, catalytic performances, compared to the density and nature of the acid sites. On the other hand, in view of a future development of bifunctional composite catalysts using the mesostructured systems reported in this work as supports to host a redox phase, the mesostructure features could play a fundamental role. Indeed, they could significantly influence the dispersion of the redox phase and its accessibility, and thus the performances of bifunctional catalysts, as already observed by other authors for mesostructured supported catalysts [63,64] and sorbents [65].

4. Conclusions

In this work three different mesostructured aluminosilicates, with different textural properties and the same Si/Al ratio (= 15) were synthesized, characterized, and tested for the CO_2-to-DME one-pot process in form of physical mixture with a commercial redox catalyst, and compared with γ-Al_2O_3, with the aim of understanding how the textural properties and the amount, strength and typology of the acid sites affect their catalytic performances for methanol dehydration to dimethyl ether. In conclusion, the following findings can be claimed:

(i) Catalysts bearing Brønsted sites, as expected, show better performances for methanol dehydration than catalysts featuring only Lewis sites. Aluminosilicates, indeed, are the catalysts which show the best performances in terms of DME selectivity (9.9–26.6 %), due to the presence of Brønsted acid sites. γ-Al_2O_3, on the other hand, due to the lack of Brønsted sites, shows significantly lower performances for methanol dehydration (S_{DME} = 1.7 %). Py-FTIR pointed out how Lewis sites have an overall higher strength than Brønsted sites, on the same sample. At high temperature (300 °C), pyridine is almost completely desorbed from Brønsted sites, while a significant amount of Lewis sites still keeps pyridine molecules adsorbed. This finding is in agreement with the higher water resistance shown by Brønsted sites.

(ii) Surface density of acid sites is a key feature to obtain good performances for methanol dehydration to DME. The three aluminosilicates, despite providing similar amounts of Brønsted sites, show significantly different catalytic performances (S_{DME} = 9.9–26.6 %). Al-SBA-16, the system with the highest methanol dehydration performances (S_{DME} = 26.6 %), also showed the highest surface density of acid sites, due to its relatively low surface area. Being methanol dehydration, indeed, a bimolecular reaction, which involves two molecules of methanol in the reaction to obtain one molecule of DME, the hypothesis which can be advanced is that the close proximity of two acid sites, on which the two needed molecules of methanol are adsorbed, may be a fundamental factor to allow a fast dehydration and thus improve DME formation.

According to our findings, an ideal dehydration catalyst should provide a high surface density of Brønsted acid sites; therefore, as a future perspective, the modification of Si/Al ratio, and particularly its decrease, should lead to the design of catalysts with enhanced performances. Furthermore, with the aim of developing bifunctional nanocomposite catalysts, the most promising mesostructured acidic systems could be used as supports to incorporate highly dispersed small nanoparticles of a Cu-based redox phase inside the mesopores. This approach should hamper the common sintering phenomena deriving from their use and, thus, improve regenerability in comparison with zeolite-based bifunctional systems.

CRediT authorship contribution statement

Fausto Secci: Conceptualization, Data curation, Formal analysis, Investigation, Methodology, Visualization, Writing – original draft. **Valentina Mameli:** Conceptualization, Data curation, Writing – review & editing. **Elisabetta Rombi:** Conceptualization, Formal analysis, Data curation, Writing – review & editing. **Sarah Lai:** Formal analysis, Writing – review & editing. **Marco Sanna Angotzi:** Data curation, Investigation, Methodology. **Patricia A. Russo:** Data curation, Formal analysis, Writing – review & editing. **Nicola Pinna:** Data curation, Writing – review & editing. **Mauro Mureddu:** Conceptualization, Methodology, Resources, Validation, Writing – review & editing. **Carla Cannas:** Conceptualization, Methodology, Visualization, Funding acquisition, Project administration, Supervision, Validation, Writing – review & editing.

Declaration of Competing Interest

The authors declare that they have no known competing financial interests or personal relationships that could have appeared to influence the work reported in this paper.

Data Availability

Data will be made available on request.

Acknowledgements

MIUR – National Program PON Ricerca e Innovazione 2014–2020 is acknowledged for the Ph.D. grant of Fausto Secci (CUP J88D19001040001). The University of Cagliari (UniCA) and Fondazione di Sardegna (FdS) are acknowledged for the financial support – Project: CUP F72F20000240007(2019): "Surface-tailored Materials for Sustainable Environmental Applications". CESA Project—RAS Piano Sulcis is gratefully acknowledged for financing the fellowships of Marco Sanna Angotzi and V. Mameli. Thanks are due to Andrea Ardu and to the "Centro Servizi di Ateneo per la Ricerca (CeSAR)" for the use of the TEM measurements performed with JEOL JEM 1400 PLUS. The catalytic tests of this study have been performed by SOTACARBO within the Advance Sustainable technologieS for Energy Transition, ASSET project (CUP D43C22002400002), funded by the Regional Government of Sardinia. Christoph Erdmann is acknowledged for transmission electron microscopy studies and EDX measurements performed with FEI TALOS F200S microscope.

Appendix A. Supporting information

Supplementary data associated with this article can be found in the online version at doi:10.1016/j.jece.2023.110018.

References

[1] E. Catizzone, G. Bonura, M. Migliori, F. Frusteri, G. Giordano, CO_2 recycling to dimethyl ether: state-of-the-art and perspectives, Molecules 23 (2018) 1–28, https://doi.org/10.3390/molecules23010031.

[2] T.A. Semelsberger, R.L. Borup, H.L. Greene, Dimethyl ether (DME) as an alternative fuel, J. Power Sources 156 (2006) 497–511, https://doi.org/10.1016/j.jpowsour.2005.05.082.

[3] J. Sun, G. Yang, Y. Yoneyama, N. Tsubaki, Catalysis chemistry of dimethyl ether synthesis, ACS Catal. 4 (2014) 3346–3356, https://doi.org/10.1021/cs500967j.

[4] J.M. Spurgeon, B. Kumar, A comparative technoeconomic analysis of pathways for commercial electrochemical CO_2 reduction to liquid products, Energy Environ. Sci. 11 (2018) 1536–1551, https://doi.org/10.1039/c8ee00097b.

[5] K. Saravanan, H. Ham, N. Tsubaki, J.W. Bae, Recent progress for direct synthesis of dimethyl ether from syngas on the heterogeneous bifunctional hybrid catalysts, Appl. Catal. B Environ. 217 (2017) 494–522, https://doi.org/10.1016/j.apcatb.2017.05.085.

[6] A. Álvarez, A. Bansode, A. Urakawa, A.V. Bavykina, T.A. Wezendonk, M. Makkee, J. Gascon, F. Kapteijn, Challenges in the greener production of formates/formic acid, methanol, and DME by heterogeneously catalyzed CO_2 hydrogenation

processes, Chem. Rev. 117 (2017) 9804–9838, https://doi.org/10.1021/acs.chemrev.6b00816.
[7] H. Ham, J. Kim, S.J. Cho, J.H. Choi, D.J. Moon, J.W. Bae, Enhanced stability of spatially confined copper nanoparticles in an ordered mesoporous alumina for dimethyl ether synthesis from syngas, ACS Catal. 6 (2016) 5629–5640, https://doi.org/10.1021/acscatal.6b00882.
[8] G.A. Olah, Towards oil independence through renewable methanol chemistry, Angew. Chem. - Int. Ed. 52 (2013) 104–107, https://doi.org/10.1002/anie.201204995.
[9] I. Miletto, E. Catizzone, G. Bonura, C. Ivaldi, M. Migliori, E. Gianotti, L. Marchese, F. Frusteri, G. Giordano, In situ FT-IR characterization of CuZnZr/ferrierite hybrid catalysts for one-pot CO_2-to-DME conversion, Materials 11 (2018), https://doi.org/10.3390/ma11112275.
[10] L. Fu, Z. Ren, W. Si, Q. Ma, W. Huang, K. Liao, Z. Huang, Y. Wang, J. Li, P. Xu, Research progress on CO_2 capture and utilization technology, J. CO_2 Util. 66 (2022), 102260, https://doi.org/10.1016/j.jcou.2022.102260.
[11] J. Wu, X.D. Zhou, Catalytic conversion of CO_2 to value added fuels: current status, challenges, and future directions, Cuihua Xuebao/Chin. J. Catal. 37 (2016) 999–1015, https://doi.org/10.1016/S1872-2067(16)62455-5.
[12] G. Bonura, M. Cordaro, C. Cannilla, A. Mezzapica, L. Spadaro, F. Arena, F. Frusteri, Catalytic behaviour of a bifunctional system for the one step synthesis of DME by CO_2 hydrogenation, Catal. Today 228 (2014) 51–57, https://doi.org/10.1016/j.cattod.2013.11.017.
[13] E. Catizzone, C. Freda, G. Braccio, F. Frusteri, G. Bonura, Dimethyl ether as circular hydrogen carrier: catalytic aspects of hydrogenation/dehydrogenation steps, J. Energy Chem. 58 (2021) 55–77, https://doi.org/10.1016/j.jechem.2020.09.040.
[14] E. Catizzone, A. Aloise, E. Giglio, G. Ferrarelli, M. Bianco, M. Migliori, G. Giordano, MFI vs. FER zeolite during methanol dehydration to dimethyl ether: the crystal size plays a key role, Catal. Commun. 149 (2021), 106214, https://doi.org/10.1016/j.catcom.2020.106214.
[15] C. Cara, F. Secci, S. Lai, V. Mameli, K. Skrodczky, P.A. Russo, F. Ferrara, E. Rombi, N. Pinna, M. Mureddu, C. Cannas, On the design of mesostructured acidic catalysts for the one-pot dimethyl ether production from CO_2, J. CO_2 Util. 62 (2022), 102066, https://doi.org/10.1016/j.jcou.2022.102066.
[16] E. Catizzone, M. Migliori, A. Purita, G. Giordano, Ferrierite vs. γ-Al_2O_3: the superiority of zeolites in terms of water-resistance in vapour-phase dehydration of methanol to dimethyl ether, J. Energy Chem. 30 (2019) 162–169, https://doi.org/10.1016/j.jechem.2018.05.004.
[17] Y. Fu, T. Hong, J. Chen, A. Auroux, J. Shen, Surface acidity and the dehydration of methanol to dimethyl ether, Thermochim. Acta 434 (2005) 22–26, https://doi.org/10.1016/j.tca.2004.12.023.
[18] N. Mota, E.M. Ordoñez, B. Pawelec, J.L.G. Fierro, R.M. Navarro, Direct synthesis of dimethyl ether from CO_2: recent advances in bifunctional/hybrid catalytic systems, Catalysts 11 (2021), https://doi.org/10.3390/catal11040411.
[19] S. Ren, X. Fan, Z. Shang, W.R. Shoemaker, L. Ma, T. Wu, S. Li, N.B. Klinghoffer, M. Yu, X. Liang, Enhanced catalytic performance of Zr modified $CuO/ZnO/Al_2O_3$ catalyst for methanol and DME synthesis via CO_2 hydrogenation, J. CO2 Util. 36 (2020) 82–95, https://doi.org/10.1016/j.jcou.2019.11.013.
[20] X. An, Y.Z. Zuo, Q. Zhang, D.Z. Wang, J.F. Wang, Dimethyl ether synthesis from CO_2 hydrogenation on a CuO-ZnO-Al_2O_3-ZrO_2/HZSM-5 bifunctional catalyst, Ind. Eng. Chem. Res. 47 (2008) 6547–6554, https://doi.org/10.1021/ie800777t.
[21] S. Ren, S. Li, N. Klinghoffer, M. Yu, X. Liang, Effects of mixing methods of bifunctional catalysts on catalyst stability of DME synthesis via CO_2 hydrogenation, Carbon Resour. Convers. 2 (2019) 85–94, https://doi.org/10.1016/j.crcon.2019.03.002.
[22] G. Bonura, M. Migliori, L. Frusteri, C. Cannilla, E. Catizzone, G. Giordano, F. Frusteri, Acidity control of zeolite functionality on activity and stability of hybrid catalysts during DME production via CO_2 hydrogenation, J. CO_2 Util. 24 (2018) 398–406, https://doi.org/10.1016/j.jcou.2018.01.028.
[23] F. Frusteri, M. Migliori, C. Cannilla, L. Frusteri, E. Catizzone, A. Aloise, G. Giordano, G. Bonura, Direct CO_2-to-DME hydrogenation reaction: new evidences of a superior behaviour of FER-based hybrid systems to obtain high DME yield, J. CO_2 Util. 18 (2017) 353–361, https://doi.org/10.1016/j.jcou.2017.01.030.
[24] C. Cara, E. Rombi, A. Musinu, V. Mameli, A. Ardu, M. Sanna Angotzi, L. Atzori, D. Niznansky, H.L. Xin, C. Cannas, MCM-41 support for ultrasmall γ-Fe_2O_3 nanoparticles for H_2S removal, J. Mater. Chem. A 5 (2017) 21688–21698, https://doi.org/10.1039/c7ta03652c.
[25] J. Wang, Q. Liu, A simple method to directly synthesize Al-SBA-15 mesoporous materials with different Al contents, Solid State Commun. 148 (2008) 529–533, https://doi.org/10.1016/j.ssc.2008.09.052.
[26] A. Ungureanu, B. Dragoi, V. Hulea, T. Cacciaguerra, D. Meloni, V. Solinas, E. Dumitriu, Effect of aluminium incorporation by the "pH-adjusting" method on the structural, acidic and catalytic properties of mesoporous SBA-15, Microporous Mesoporous Mater. 163 (2012) 51–64, https://doi.org/10.1016/j.micromeso.2012.05.007.
[27] D. Meloni, D. Perra, R. Monaci, M.G. Cutrufello, E. Rombi, I. Ferino, Transesterification of Jatropha curcas oil and soybean oil on Al-SBA-15 catalysts, Appl. Catal. B Environ. 184 (2016) 163–173, https://doi.org/10.1016/j.apcatb.2015.11.038.
[28] Q. Yuan, A.X. Yin, C. Luo, L.D. Sun, Y.W. Zhang, W.T. Duan, H.C. Liu, C.H. Yan, Facile synthesis for ordered mesoporous γ-aluminas with high thermal stability, J. Am. Chem. Soc. 130 (2008) 3465–3472, https://doi.org/10.1021/ja0764308.
[29] H. Ding, H. Sun, Y. Shan, Preparation and characterization of mesoporous SBA-15 supported dye-sensitized TiO_2 photocatalyst, J. Photochem. Photobiol. A Chem. 169 (2005) 101–107, https://doi.org/10.1016/j.jphotochem.2004.04.015.
[30] G.F. Andrade, D.C.F. Soares, R.K.D.S. Almeida, E.M.B. Sousa, Mesoporous silica SBA-16 functionalized with alkoxysilane groups: preparation, characterization, and release profile study, J. Nanomater 2012 (2012), https://doi.org/10.1155/2012/816496.
[31] V. Palos-Barba, A. Moreno-Martell, V. Hernández-Morales, C.L. Peza-Ledesma, E. M. Rivera-Muñoz, R. Nava, B. Pawelec, SBA-16 cage-like porous material modified with APTES as an adsorbent for Pb^{2+} ions removal from aqueous solution, Materials 13 (2020) 1–15.
[32] L. Lutterotti, P. Scardi, Simultaneous structure and size-strain refinement by the rietveld method, J. Appl. Crystallogr. 23 (1990) 246–252, https://doi.org/10.1107/S0021889890002382.
[33] K. Shirasuka, H. Yanagida, G. Yamaguchi, The preparation of η alumina and its structure, J. Ceram. Assoc. Jpn. 84 (1976) 610–613, https://doi.org/10.2109/jcersj1950.84.976_610.
[34] L. Wang, J. Fan, B. Tian, H. Yang, C. Yu, B. Tu, D. Zhao, Synthesis and characterization of small pore thick-walled SBA-16 templated by oligomeric surfactant with ultra-long hydrophilic chains, Microporous Mesoporous Mater. 67 (2004) 135–141, https://doi.org/10.1016/j.micromeso.2003.10.015.
[35] P. Van Der Voort, M. Benjelloun, E.F. Vansant, Rationalization of the synthesis of SBA-16: controlling the micro- and mesoporosity, J. Phys. Chem. B 106 (2002) 9027–9032, https://doi.org/10.1021/jp0261152.
[36] C.A. Emeis, Determination of integrated molar extinction coefficients for IR absorption bands of pyridine adsorbed on solid acid catalysts, J. Catal. 141 (1993) 347–354, https://doi.org/10.1002/chin.199338056.
[37] G. Lombardelli, M. Mureddu, S. Lai, F. Ferrara, A. Pettinau, L. Atzori, A. Conversano, M. Gatti, CO_2 hydrogenation to methanol with an innovative Cu/Zn/Al/Zr catalyst: experimental tests and process modeling, J. CO2 Util. 65 (2022), 102240, https://doi.org/10.1016/j.jcou.2022.102240.
[38] D. Zhao, Y. Wan, W. Zhou, Ordered Mesoporous Materials, Wiley-VCH, 2013, https://doi.org/10.1002/9783527647866.
[39] G.L. Seah, L. Wang, L.F. Tan, C. Tipjanrawee, W.A. Sasangka, A.K. Usadi, J. M. McConnachie, K.W. Tan, Ordered mesoporous alumina with tunable morphologies and pore sizes for CO_2 capture and dye separation, ACS Appl. Mater. Interfaces 13 (2021) 36117–36129, https://doi.org/10.1021/acsami.1c06151.
[40] Q. Yuan, H.H. Duan, L. Le Li, Z.X. Li, W.T. Duan, L.S. Zhang, W.G. Song, C.H. Yan, Homogeneously dispersed ceria nanocatalyst stabilized with ordered mesoporous alumina, Adv. Mater. 22 (2010) 1475–1478, https://doi.org/10.1002/adma.200904223.
[41] J. Socci, A. Osatiashtiani, G. Kyriakou, T. Bridgwater, The catalytic cracking of sterically challenging plastic feedstocks over high acid density Al-SBA-15 catalysts, Appl. Catal. A Gen. 570 (2019) 218–227, https://doi.org/10.1016/j.apcata.2018.11.020.
[42] R.M. Grudzien, B.E. Grabicka, M. Jaroniec, Adsorption and structural properties of channel-like and cage-like organosilicas, Adsorption 12 (2006) 293–308, https://doi.org/10.1007/s10450-006-0560-2.
[43] Q. Wu, F. Zhang, J. Yang, Q. Li, B. Tu, D. Zhao, Synthesis of ordered mesoporous alumina with large pore sizes and hierarchical structure, Microporous Mesoporous Mater. 143 (2011) 406–412, https://doi.org/10.1016/j.micromeso.2011.03.033.
[44] K. Niesz, P. Yang, G.A. Somorjai, Sol-gel synthesis of ordered mesoporous alumina, Chem. Commun. (2005) 1986–1987, https://doi.org/10.1039/b419249d.
[45] G.D.S. Peidong Yang, Dongyuan Zhao, David I. Margolese, Bradley F. Chmelka, Block copolymer templating syntheses of mesoporous metal oxides with large ordering lengths and semicrystalline framework, Chem. Mater., vol. 1536, 1999, pp. 2813–26. ⟨https://doi.org/10.1063/1.4810413⟩.
[46] P. Carta, C. Cara, C. Cannas, M.A. Scorciapino, Experiments-guided modeling of MCM-41: impact of pore symmetry on gas adsorption, Adv. Mater. Interfaces 9 (2022), 2201591, https://doi.org/10.1002/admi.202201591.
[47] Y. Li, W. Zhang, L. Zhang, Q. Yang, Z. Wei, Z. Feng, C. Li, Direct synthesis of Al-SBA-15 mesoporous materials via hydrolysis-controlled approach, J. Phys. Chem. B 108 (2004) 9739–9744, https://doi.org/10.1021/jp049824j.
[48] S. Xing, P. Lv, J. Fu, J. Wang, P. Fan, L. Yang, Z. Yuan, Direct synthesis and characterization of pore-broadened Al-SBA-15, Microporous Mesoporous Mater. 239 (2017) 316–327, https://doi.org/10.1016/j.micromeso.2016.10.018.
[49] K. Góra-Marek, M. Derewiński, P. Sarv, J. Datka, IR and NMR studies of mesoporous alumina and related aluminosilicates, Catal. Today 101 (2005) 131–138, https://doi.org/10.1016/j.cattod.2005.01.010.
[50] M.L. Occelli, S. Biz, A. Auroux, G.J. Ray, Effects of the nature of the aluminum source on the acidic properties of some mesostructured materials, Microporous Mesoporous Mater. 26 (1998) 193–213, https://doi.org/10.1016/S1387-1811(98)00201-7.
[51] J.N. Kondo, R. Nishitani, E. Yoda, T. Yokoi, T. Tatsumi, K. Domen, A comparative IR characterization of acidic sites on HY zeolite by pyridine and CO probes with silica-alumina and γ-alumina references, Phys. Chem. Chem. Phys. 12 (2010) 11576–11586, https://doi.org/10.1039/c0cp00203h.
[52] Y. Matsunaga, H. Yamazaki, T. Yokoi, T. Tatsumi, J.N. Kondo, IR characterization of homogeneously mixed silica-alumina samples and dealuminated y zeolites by using pyridine, CO, and propene probe molecules, J. Phys. Chem. C 117 (2013) 14043–14050, https://doi.org/10.1021/jp403242n.
[53] J.M.R. Gallo, C. Bisio, G. Gatti, L. Marchese, H.O. Pastore, Physicochemical characterization and surface acid properties of mesoporous [Al]-SBA-15 obtained by direct synthesis, Langmuir 26 (2010) 5791–5800, https://doi.org/10.1021/la903661q.
[54] Y.F. Shen, S.L. Suib, M. Deeba, G.S. Koermer, Luminescence and IR characterization of acid sites on alumina, J. Catal. 146 (1994) 483–490, https://doi.org/10.1006/jcat.1994.1086.

[55] M.R. Gafurov, I.N. Mukhambetov, B.V. Yavkin, G.V. Mamin, A.A. Lamberov, S. B. Orlinskii, Quantitative analysis of Lewis acid centers of γ-alumina by using EPR of the adsorbed anthraquinone as a probe molecule: comparison with the pyridine, carbon monoxide IR, and TPD of ammonia, J. Phys. Chem. C 119 (2015) 27410–27415, https://doi.org/10.1021/acs.jpcc.5b09759.

[56] X. Liu, R.E. Truitt, DRFT-IR studies of the surface of γ-alumina, J. Am. Chem. Soc. 119 (1997) 9856–9860, https://doi.org/10.1021/ja971214s.

[57] M.I. Zaki, M.A. Hasan, F.A. Al-sagheer, L. Pasupulety, In situ FTIR spectra of pyridine adsorbed on SiO_2–Al_2O_3, TiO_2, ZrO_2 and CeO_2: general considerations for the identification of acid sites on surfaces of finely divided metal oxides, Colloids Surf. 190 (2001) 261–274.

[58] N. Cardona-Martinez, J.A. Dumesic, Applications of adsorption microcalorimetry to the study of heterogeneous catalysis, Adv. Catal. 38 (1992) 149–244, https://doi.org/10.1016/S0360-0564(08)60007-3.

[59] B. Dragoi, A. Gervasini, E. Dumitriu, A. Auroux, Calorimetric determination of the acidic character of amorphous and crystalline aluminosilicates, Thermochim. Acta 420 (2004) 127–134, https://doi.org/10.1016/j.tca.2003.10.031.

[60] B. Spiewak, B. Handy, S. Sharma, J. Dumesic, Microcalorimetric studies of ammonia adsorption on γ-Al_2O_3, HNa-Y zeolite, and H-mordenite, Catal. Lett. 23 (1994) 207–213.

[61] O.C. Gobin, Q. Huang, H. Vinh-Thang, F. Kleitz, M. Eić, S. Kaliaguine, Mesostructured silica SBA-16 with tailored intrawall porosity Part 2: diffusion, J. Phys. Chem. C 111 (2007) 3059–3065, https://doi.org/10.1021/jp063583t.

[62] J. Fan, C. Yu, L. Wang, B. Tu, D. Zhao, Y. Sakamoto, O. Terasaki, Mesotunnels on the silica wall of ordered SBA-15 to generate three-dimensional large-pore mesoporous networks [15], J. Am. Chem. Soc. 123 (2001) 12113–12114, https://doi.org/10.1021/ja011564l.

[63] A.E. Barrón Cruz, J.A. Melo Banda, H. Mendoza, C.E. Ramos-Galvan, M.A. Meraz Melo, D. Esquivel, Pt and Ni supported catalysts on SBA-15 and SBA-16 for the synthesis of biodiesel, Catal. Today 166 (2011) 111–115, https://doi.org/10.1016/j.cattod.2011.01.008.

[64] R. Huirache-Acuña, B. Pawelec, E. Rivera-Muñoz, R. Nava, J. Espino, J.L.G. Fierro, Comparison of the morphology and HDS activity of ternary Co-Mo-W catalysts supported on P-modified SBA-15 and SBA-16 substrates, Appl. Catal. B Environ. 92 (2009) 168–184, https://doi.org/10.1016/j.apcatb.2009.07.012.

[65] C. Cara, E. Rombi, V. Mameli, A. Ardu, M. Sanna Angotzi, D. Niznansky, A. Musinu, C. Cannas, γ-Fe_2O_3-M41S sorbents for H_2S removal: effect of different porous structures and silica wall thickness, J. Phys. Chem. C 122 (2018) 12231–12242, https://doi.org/10.1021/acs.jpcc.8b01487.